Experimental and theoretical studies on turbulent mixing of two confined jets

T.-M. Liou, K.-L. Hsiao and M.-K. Tsai
Department of Power Mechanical Engineering, National Tsing Hua University, Taiwan, ROC

A study of turbulent mixing of two confined jets in a side-dump combustor was carried out with complementary numerical and experimental efforts. The side-inlet angle was varied from 15° to 135°, air-to-fuel ratio from 1.8 to 6.4, and combustor Reynolds number from 1.1×10^4 to 5.9×10^4, respectively, to investigate their effects on the flow and mixing patterns. The fuel concentration distribution calculated from the temperature measurements using the Mach-Zehnder interferometry and thermocouple probing is in good agreement with that predicted with an algebraic Reynolds stress turbulence model. The side-inlet angle is found to affect largely the dominant role played by the jet impingement or entrainment. The existence of the critical side-inlet angle and Reynolds number and the increase of uniformity of mixing with increasing air-to-fuel ratio are believed to be useful for the design of side-dump combustors.

Keywords: turbulent mixing; noncoaxial jets; side-dump combustor; Mach-Zehnder interferometry

Introduction

The flow and concentration patterns of sudden-expansion dump-type combustors, which are used in ramjets,[1] turbojets,[2] industrial furnaces,[3] and the mixing chamber of gas-fired pulsating combustors,[4] are mainly characterized by the turbulent mixing of two confined jets. Most of the previous efforts are on the coaxial-dump combustors.[3,5,6] In contrast, fundamental research on the side-dump combustors (Figures 1 and 2) is limited. In the side-dump combustors, fluid mixing and combustion process are additionally affected by the jet impingement since the fuel and air jets in such combustors are often not coaxial. Therefore, an understanding of the complex flow and mixing patterns involved in the side-dump combustors is important to improving combustion performance. In the present work we thus focus on the side-dump combustors.

The effects of geometric and/or aerodynamic parameters on the flow patterns, temperature and/or fuel fraction distributions, and specific impulse or combustion efficiency of the combustors with side air and axial fuel inlets were theoretically analyzed by Chen and Tao,[7] Vanka et al.,[8] Cherng et al.,[9] and Hwang.[10] Among these studies, Chen and Tao solved the two-dimensional (2-D) reacting flow equations and the others 3-D. These studies provided useful information to the understanding of flow and combustion processes in the side-dump combustors. Nevertheless, no model validation was made in all these studies due to the lack of direct comparison with experimental data.

Schadow and Chieze[11] performed windowed combustor and water tunnel tests. From the water flow and flame characteristics qualitative insight was gained by them into the effect of air inlet momentum, fuel injection momentum, and air inlet angle on combustion efficiency. Zetterström and Sjöblom[12] carried out water-tunnel and combustion tests to provide stability performance data, combustion efficiency data, and pressure oscillation data for a side-dump combustor with fuel injection in the combustor inlet. A vane was found to be required in the combustor inlet in order to provide a stable flow pattern. No comparison with theoretical computation was made in the above two experimental investigations. Stull et al.[13] and recently Liou et al.[14–16] conducted flow visualization studies and laser-Doppler velocimetry (LDV) measurements, respectively, for the side-dump combustors without the axial fuel inlet. Their flow-field results were used to validate the corresponding combustor flow models.

The brief survey just given indicates that direct comparisons between the experimental and theoretical results relevant to the side-dump combustors are scarce. The quantitative comparisons of the measured and calculated noncoaxial mixing patterns that characterize the side-dump combustors are especially lacking, and this has motivated the present work. In the present study, as a continuation of our previous work[15,16] and as an intermediate step to understand the actual mixing mechanisms accompanied by chemical reactions, a simplified rectangular model combustor involving no chemical reaction was constructed to provide experimental data on the mixing between two noncoaxial jets and to provide the necessary data for the input of theoretical predictions.

In the present work, the concentration measurements were performed by the temperature tracer technique. Temperature measurements were carried out with complementary thermocouple probing and nonintrusive laser Mach-Zehnder interferometry. The method of calculation employed the algebraic Reynolds stress model, which has been previously proven to be appropriate for predicting the flow fields in cylindrical ramjet combustors with two side inlets.[15] A combustor with a rectangular cross section was chosen since it allows the 2-D laser Mach-Zehnder interferometry to be performed and allows the measured data to validate our 2-D computer code. The main parameters investigated were the side-inlet angle, the mass or momentum ratio of the two jets, and the Reynolds number.

In the following sections, the experimental system and conditions are described first. The details of theoretical treatment, including the equations solved, boundary conditions specified, and solution algorithm used, are stated subsequently. The computed flow and mixing patterns for different side-inlet

Address reprint requests to Professor Tong-Miin Liou at the Department of Power Mechanical Engineering, National Tsing Hua University, Hsinchu, Taiwan 30043, ROC.

Received 1 December 1989; accepted 31 January 1991

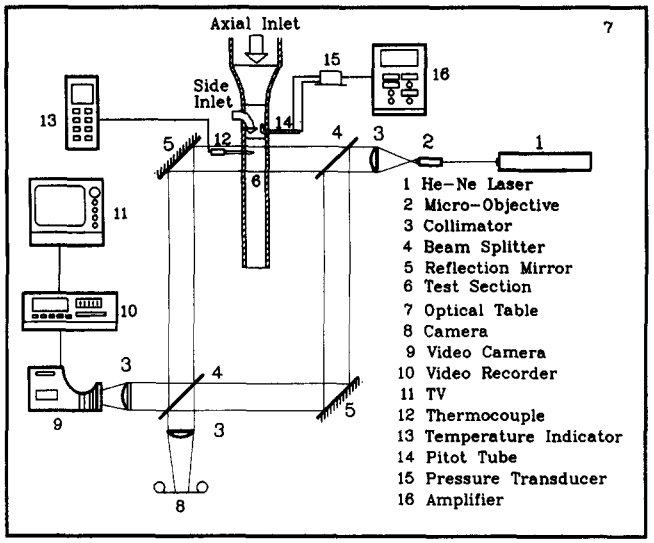

Figure 1 Schematic drawing of overall experimental system

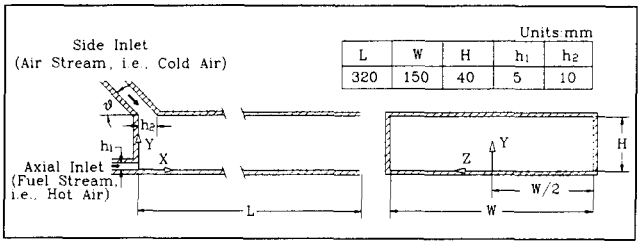

Figure 2 Sketch of configuration, coordinate system, and dimensions of the test section

angles, air-to-fuel mass ratios, and Reynolds numbers are then discussed. Moreover, detailed comparison between the calculated and measured results is made under different air-to-fuel mass ratios.

Experimental system and conditions

Experimental system

The model combustor, Pitot tube, thermocouple probing, and laser Mach-Zehnder interferometer setup is shown schematically in Figure 1. The test section was provided with two inlets, i.e., a side inlet and an axial one, as shown in Figures 1 and 2. Air was forced into the side inlet through a rotameter, a diffuser, a flow straightener, and five screens (mesh number of 60 or 4.2×10^{-4} m, square pattern, and void fraction of 0.587) in the settling chamber and a bellmouth contraction (10.3:1) by a 5-hp centrifugal blower. The air then dumped into the test section through the side port. This side-inlet stream will be referred to as the air stream in the present work. A similar arrangement was made for the second air stream, which was dumped into the test section through the axial inlet after being heated using an electric heater. This second hot air stream was intended to simulate the fuel stream and, therefore, will be referred to as the fuel stream in this study. Downstream of the test section, the mixed air streams then flowed through a flow straightener and a bellows and was exhausted into the atmosphere.

The temperature tracer technique was used to convert the temperature data to the concentration data of the fuel stream at different points inside the test section through the following relation[3,17]:

$$F=(T-T_a)/(T_f-T_a)=m_f/(m_f+m_a)$$

where F is the mixture fraction or the mass concentration of the fuel stream and T_f, T_a are the temperatures of the fuel and air streams at inlets to the model combustor, m_f and m_a are the local masses of the fuel and air streams at the point considered. Two techniques, thermocouple probing and laser Mach-Zehnder interferometry, were used to measure the local temperatures (T) of the gas mixture. Copper-constantan thermocouples, made of 0.25-mm diameter wires, were used for temperature traverses across nine axial stations that were located at $X/H=0.00$, 0.25, 0.50, 0.75, 1.00, 1.25, 1.50, 1.75, and 3.50, respectively. In each station the measurements were

Notation

$C_1, C_2, C_{A1}, C_{A2}, C_\mu$	Constants in turbulence model
F	Mixture fraction or fuel concentration
F_B	Bulk mean value of F at a given axial station
H	Combustor height
H_r	Height of recirculating zone
h_1	Width of axial-inlet port
h_2	Width of side-inlet port
k	Turbulence kinetic energy
L	Combustor length
L_r	Reattachment length
m_a	Local mass (fraction) of air stream
m_f	Local mass (fraction) of fuel stream
P	Pressure
Re	Combustor Reynolds number, $\mathrm{Re}=\rho U_B H/\mu_l$
S	Deviation of fuel concentration from the local bulk mean value at a given axial station
T	Local mixture temperature
T_a	Temperature of air stream at side-inlet port
T_f	Temperature of fuel stream at axial-inlet port
U	Axial mean velocity
U_B	Combustor bulk mean velocity
U_{max}	Maximum mean velocity at axial-inlet port
V	Transverse mean velocity
V_{max}	Maximum mean velocity at side-inlet port
W	Combustor width
X	Axial coordinate
Y	Transverse coordinate
Z	Spanwise coordinate
Greek symbols	
ε	Dissipation rate of turbulence kinetic energy
θ	Side-inlet angle, i.e., angle between side-inlet duct and negative X-axis
ρ	Fluid density
μ_l	Molecular dynamic viscosity
μ_t	Turbulent dynamic viscosity
$\sigma_k, \sigma_\varepsilon$	Turbulent Prandtl number of k and ε, respectively

made at 18 locations from $Y/H=0$ to 1. The positioning accuracy of the thermocouple bead was ± 0.1 mm. For the case of laser Mach-Zehnder interferometry, the temperature measurements were noninvasive. The beam of a 15-mV helium-neon laser (632.8 nm wavelength) was expanded and split into two beams of 15-mm diameter with plane wave fronts. The test beam passed through the test section, and the reference beam bypassed it. The expanded test beam would be distorted as a result of the refracted index field generated by local temperature variation in the test section. The distorted test beam subsequently recombined with the reference beam at the second beam splitter located behind the test section. The recombined beams then passed on to the screen or video camera on which an instantaneous interference field formed. The instantaneous interference field was monitored on a TV as well as videotaped with a shutter camera and recorded on a VHS videocassette recorder for storage and analysis.

To determine the temperature field described by the image of interferogram the equation of interferometry for a 2-D incompressible flow is as follows[18]:

$$S_i - S_{i-1} = \frac{T_r \rho_r C W}{\lambda}\left(\frac{1}{T_{S_i}} - \frac{1}{T_{S_{i-1}}}\right)$$

where $S_i - S_{i-1}$ is the fringe shift, S_i the fringe order, C the Gladstone-Dale constant, W the combustor width, λ the laser wavelength, and ρ_r the air density evaluated at reference temperature T_r. By setting $S_i - S_{i-1} = 1$, the temperature differences $T_{S_i} - T_{S_{i-1}}$ associated with each fringe were determined. The image was calibrated by confirming the reasonable agreement between the interferometric data and the well-known universal temperature profile in the near wall region of a smooth duct.[19] In addition, various linear and nonlinear image processing functions (Imaging Technology, Inc.) were used to analyze, enhance, and modify entire images or selected parts of an image. For instance, binarization by thresholding technique was adopted for background noise subtraction, 16 consecutive images were added and averaged to reduce the optical and electronic noises, and median filtering was performed to reduce spot or point noise. These functions were all carried out by matrix–matrix convolution operations.

Additionally, a Pitot tube of 1.6-mm diameter was used to measure the mean velocity profiles at the above mentioned two inlet ports. These velocity data then provided the boundary conditions for the subsequent computations.

Model combustor

The test section was a model combustor whose configuration and coordinate system are presented in Figure 2. The internal dimensions of the axial and side inlets were 5×150 ($Y \times Z$) mm^2 and 10×150 ($X \times Z$) mm^2, respectively. The rectangular combustion chamber had a cross-sectional area of 40×150 ($Y \times Z$) mm^2 and was 320-mm long. The axial inlet duct was well insulated by fiberglass material and the rectangular combustion chamber by a combination of 5-mm thick Bakelite and 20-mm thick foam rubber. Both side walls of the model combustor had quartz windows to provide optical access for laser Mach-Zehnder interferometry measurements.

Experimental conditions

The Reynolds number, based on the combustor height (H) and bulk mean velocity (U_B), was varied from 1.1×10^4 to 5.9×10^4. The corresponding bulk mean velocity values for the side-inlet (U_a) and axial (U_f) ports were from 18.3 to 35.4 m/sec and 12.2 to 22.6 m/sec, respectively. Also the air-to-fuel mass ratios tested were A/F = 1.8, 3.4, 4.0, 4.6, and 6.4. The corresponding equivalence ratios and momentum-flux ratios of air and fuel jets were 1.8, 0.9, 0.8, 0.7, 0.5, and $(\dot{m}\,V)_a/(\dot{m}\,V)_f = 18.3$, 9.4, 7.1, 5.1, 1.5, respectively. The variation of air to fuel mass ratio was achieved by adjusting the blower speed for the air or fuel stream. The simulated fuel was the solid propellant gas with composition of 50 percent polyester and 50 percent ammonium perchlorate by weight.[7] The stoichiometric air-to-fuel ratio is 3.2. In addition, the geometric parameter investigated numerically was the side-inlet angle, which was varied from 15° to 135°. In the present work, the baseline case selected had A/F = 4.0, $\mathrm{Re} = 1.75 \times 10^4$ ($U_B = 7.1$ m/sec), $U_a = 22.1$ m/sec, $U_f = 12.4$ m/sec, and $\theta = 90°$.

Theoretical analysis

Governing equations

The time-averaged equations for conservation of mass and momentum, the algebraic Reynolds stress equations, and the differential equations for k and its dissipation rate ε are listed in detail in another article.[15] However, one of the main purposes of this study is to provide concentration information. To this end the mass-fraction equation, which governs the distribution of mass fraction of fuel and air, has to be additionally solved.

$$\frac{\partial}{\partial X_j}(\rho U_j F) = \frac{\partial}{\partial X_j}\left[\left(\mu_l + \frac{\mu_t}{S_{ct}}\right)\frac{\partial F}{\partial X_j}\right]$$

where $S_{ct} = 0.7$ is the turbulent Schmidt number.

Boundary conditions

The governing set of partial differential equations has to be solved with the following boundary conditions:

(1) Side air inlet

$U = 0$; $V =$ measured V_{in}; $F = 0$

$k = k_{\mathrm{in}} = 0.03 V_{\mathrm{in}}^2$; $\varepsilon = \varepsilon_{\mathrm{in}} = k_{\mathrm{in}}^{3/2}/(\lambda h_2)$, where $\lambda = 0.03$

The dimensionless turbulence length scale λ was determined by the characteristic mesh size of the screens in the settling chamber and by the 10.3:1 contraction of the bellmouth entry, which is situated upstream of each inlet duct. The computed results were found to be insensitive to λ ranged from 0.003 to 0.03.

(2) Axial fuel inlet

$U =$ measured U_{in}; $V = 0$; $F =$ measured F_{in}

$k = k_{\mathrm{in}} = 0.03 U_{\mathrm{in}}^2$; $\varepsilon = \varepsilon_{\mathrm{in}} = k_{\mathrm{in}}^{3/2}/(\lambda h_1)$, where $\lambda = 0.03$

The downstream boundary was determined from the computational test, which showed that there was no noticeable change in the flow field as long as the location of the exit plane was far enough to allow the flow becoming unidirectional.

(3) Exit

$$\frac{\partial U}{\partial X} = \frac{\partial F}{\partial X} = \frac{\partial k}{\partial X} = \frac{\partial \varepsilon}{\partial X} = 0; \quad V = 0$$

(4) Walls

Since the k and ε equations are valid only in those regions that are strongly turbulent, it is not applicable in the viscous sublayer. In addition, to avoid the need for detail calculations in the near-wall regions, the wall functions[20,21] were introduced to link the values of dependent variables on the wall to those in the logarithmic region. The wall values for F were calculated from the measured wall temperatures.

Numerical scheme

The finite difference and numerical schemes have been described in detail elsewhere.[15] For selecting a reasonable nonuniform grid system, a grid refinement test was performed with three kinds of grids, i.e., 85 (axial) × 30 (transverse), 49 × 23, and 37 × 10. A large difference in the computed results was found between 37 × 10 and 85 × 30. However, the computed results for the 49 × 23 grid were nearly identical to those for the 85 × 30 grid. The calculations of this study then were made using a 49 × 23 grid, which is close to the grid density adopted in our previous study[16] for the case of modeling the turbulent flow field in a rectangular combustor with two side inlets. Typically, convergence required 600 iterations and the corresponding CPU time on a CDC-CYBER 180/840 computer system was about 3.5 hours.

Results and discussion

Computed flow and mixing patterns

The computed results for various side-inlet angles are based on the assumed uniform inlet profiles for both mean velocity and temperature and on the adiabatic wall condition. Figures 3–5 depict the calculated mean flow streamlines and fuel concentration contours of three typical side-inlet angles (θ): 60°, 45°, and 30°, for A/F = 4.0 and Re = 1.89×10^4. For $\theta = 60°$ (Figure 3a), the interaction of two jets is dominated by the jet impingement. The side air jet first impinges on the axial fuel jet and then is bent toward the downstream direction. At the downstream edge ($X/H = 0.25$) of the side-inlet port, the air jet separates due to sudden expansion and then reattaches to the upper side wall ($Y/H = 1.0$), forming a large recirculating zone.

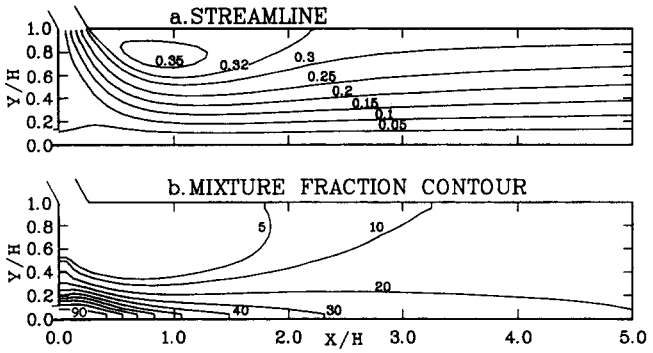

Figure 3 Calculated (a) mean flow streamlines; (b) fuel concentration contours ($\theta = 60°$, A/F = 4.0, Re = 1.89×10^4)

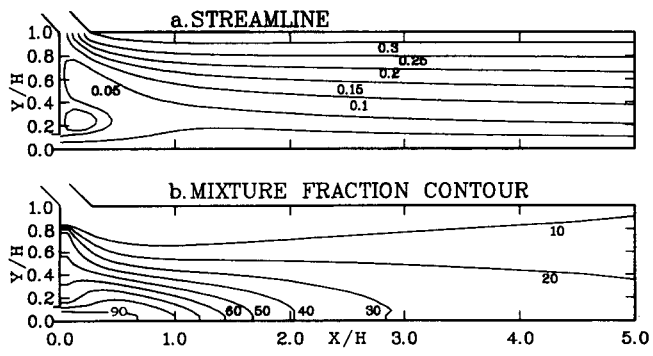

Figure 4 Calculated (a) mean flow streamlines; (b) fuel concentration contours ($\theta = 45°$, A/F = 4.0, Re = 1.89×10^4)

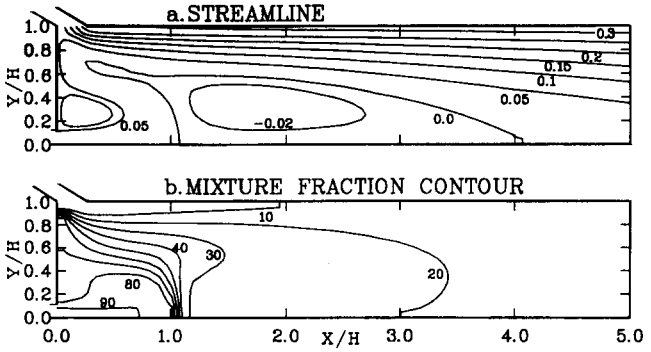

Figure 5 Calculated (a) mean flow streamlines; (b) fuel concentration contours ($\theta = 30°$, A/F = 4.0, Re = 1.89×10^4)

The aforementioned jet impingement confines the axial fuel jet to flow along the bottom side wall ($Y/H = 0.0$) and leads to steep concentration gradients prevailing in the impingement zone (Figure 3b). The intersection point, about at $X/H = 4.2$, of the stoichiometric concentration contour $F = 23.8$ percent with the bottom side wall may provide the information of flame length.[3,7,8] In addition, the uniform concentration distribution in the recirculating zone illustrates the fact that the large recirculating flow provides a good mechanism for mixing.

As θ decreases from 60° to 45° (Figure 4a), the axial velocity component of the side-inlet air jet increases and, hence, the jet entrainment is starting to play a more important role. Note that the large recirculating zone on the upper wall side occurring in the case of $\theta = 60°$ is no longer appearing here. Instead, the sudden expansion causes the axial fuel jet to separate at the upper edge of the axial-inlet port and to form a small recirculating zone between the two inlet ports and near the head-end wall. Outside of the recirculating zone, part of fuel flow expanded upward is forced to turn downstream by the entrainment of the air jet. The fuel concentration contours as shown in Figure 4b indicate a broader steep-gradient region and a longer flame length, as compared with the case of $\theta = 60°$. Again, the presence of the small recirculating zone helps the mixing, although not much due to its small size.

For the case of $\theta = 30°$ the axial fuel jet has a larger space for sudden expansion, as compared with the case of $\theta = 45°$, and, hence, a larger recirculating zone forming on the head-wall side. Moreover, Figure 5a shows that the flow field is mainly controlled by the entrainment of the fuel into the side air jet. In fact, the entrainment effect is so large that the whole fuel jet is forced to separate from the bottom side wall and bend upward to interact with the air jet. Once the two jets join together, they proceed downstream. The separated fuel jet subsequently reattaches to the bottom side wall at about $X/H = 4.1$, forming a relatively large recirculating zone. It is due to the existence of the above two recirculating zones that the steep concentration gradients can only prevail in the region between the two recirculating zones, as shown in Figure 5b. The resulting flame length at this side-inlet angle is the shortest, about $X/H = 2.1$, among the three cases shown in Figures 3–5.

Effect of side-inlet angle

Figures 3–5 just presented have clearly revealed the important role played by the side-inlet angle in establishing the flow and mixing characteristics. The size and position of the recirculating zones are shown to vary with the side-inlet angle since θ determines directly the interactions between the side air and axial fuel jets. More specifically, the normalized length (L_r/H) and height (H_r/H) of the large recirculating zone on the bottom ($Y/H = 0.0$, $\theta < 45°$) or upper ($Y/H = 1.0$, $\theta > 45°$) wall side are

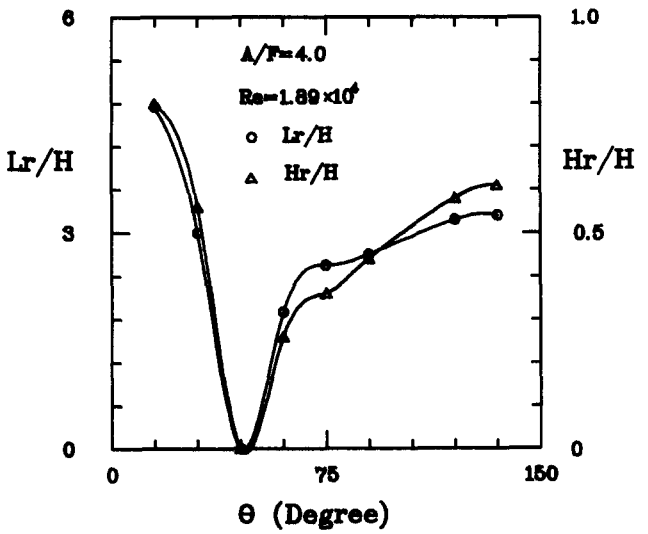

Figure 6 Effect of side-inlet angle on the calculated length and height of the recirculating zone

plotted versus θ in Figure 6. The results show an increase in L_r/H and H_r/H with increasing side-inlet angle for $\theta > 45°$ and with decreasing side-inlet angle for $\theta < 45°$, respectively. $\theta = 45°$ is found to be a critical angle above which the time-averaged position of the large recirculation zone is shifted from the bottom wall side to the upper wall side. However, it may be worth keeping in mind that, although the time-averaged length and height of the recirculating zone are zero for $\theta = 45°$, the transient nature of the real flow would cause the recirculation bubble to alternate back and forth between its upper and lower, time-averaged locations.

A comparison of the uniformity of the fuel concentration distribution at each axial station may provide information on the relative magnitude of the flame length. To represent the concentration uniformity at a given axial station, the fuel concentrations are averaged over the whole station, i.e., from $Y/H = 0$ to $Y/H = 1.0$, and the corresponding deviation, S, is calculated according to the following expression:

$$S = \Sigma[(F - F_B)^2/(N-1)]^{1/2}$$

where N is the number of data points used in Y-direction.

Thus, a smaller value of S will represent a more uniform fuel concentration distribution across the station. The results are plotted versus normalized axial coordinate in Figure 7 for various side-inlet angles. As one expects, the uniformity of mixing increases with the axial distance ($X/H \geq 1.0$) as indicated by the monotonic decrease of S with increasing X/H. Steep variations of S are found between $X/H = 0$ and $X/H = 2.5$, i.e., the jet interaction region, for all θ interested. Note that the curves for $\theta \leq 60°$ reveal a decrease of S from their peak values located between $0 < X/H < 1.0$ as X/H decreases toward the head wall ($X/H = 0$). This decrease of S is due to the presence of the foregoing mentioned small recirculating zone near the head wall. In addition, Figure 7 shows that the uniformity of mixing, in general, increases with increasing θ for $\theta > 45°$ and with decreasing θ for $\theta < 45°$, respectively. In fact, the trend shown in Figure 7 is consistent with that shown in Figure 6 since the recirculating flow provides a good mechanism for mixing. For $\theta = 45°$ the mean flow field lacks of aforementioned upper or lower recirculating zone and, hence, it has the greatest variance S in mixture fraction (Figure 7, $X/H > 0.5$). Nevertheless, it should be pointed out that the angle at which S_{max} occurs depends on the momentum ratio and the ratio of the slot widths as well. For example, previous studies of the limiting cases, $h_i/H = 1^{22}$ and $h_i/H = 0^2$ indicated the absence of recirculation zones near the head wall ($X/H = 0$) and bottom wall ($Y/H = 0$) due to the lack of axial sudden-expansion. In these limiting cases S_{max} would not occur at $\theta = 45°$. In addition, the flowfield study in Ref. 22 showed the insensitivity of flow pattern to the ratio of the exiting boundary layer thicknesses that develop inside the axial- and fuel-inlet ports.

For a diffusion flame, the concentration gradients are the steepest across the flame front and, hence, the S value in Figure 7 will be large for each axial station that cuts across the flame. Consequently, the relative magnitude of S value of different θ at a given X/H (for $X/H > 2.5$, say) may indicate the relative magnitude of flame length of different θ. The trend shown in Figure 7 is then the decrease of flame length with increasing θ for $\theta > 45°$ and with decreasing θ for $\theta < 45°$, respectively. This observation is consistent with that previously made from Figures 3–5.

Although the uniformity of fuel concentration at various streamwise stations can be characterized by the aforementioned S, the information on the local strength of mixing between the fuel and air streams is more appropriately provided by the fuel-jet width and mass entrainment. As an example, Figure 8 includes the mean-velocity vector plot and contour, the fuel-jet width (defined as the transverse distance between Y_m where $U = U_{max}$ and $Y_{0.5}$ where $U = 1/2U_{max}$), and the rate of mass entrainment for the case $\theta = 90°$. It is seen that the flow pattern displayed by Figure 8a is similar to that shown by the streamline plot in Figure 3 for $\theta = 60°$. The greatly distorted contour plot depicted by Figure 8b reveals significant difference from that of a 2-D wall jet. The difference from a 2-D wall jet can be further illustrated by Figures 8c and 8d. The spread of the present fuel jet (Figure 8c) first increases abruptly at a short distance downstream of the fuel-port due to the effect of the side air jet and then gradually parallels that of a 2-D wall jet as $X > 1.0$. Consequently, the rate of mass entrainment (Figure 8d) is largest in the region $X/H < 1$, as had been judged from Figures 3–5.

Comparison between computations and measurements

The computations for various air-to-fuel mass or momentum ratios are based on the measured inlet conditions shown in

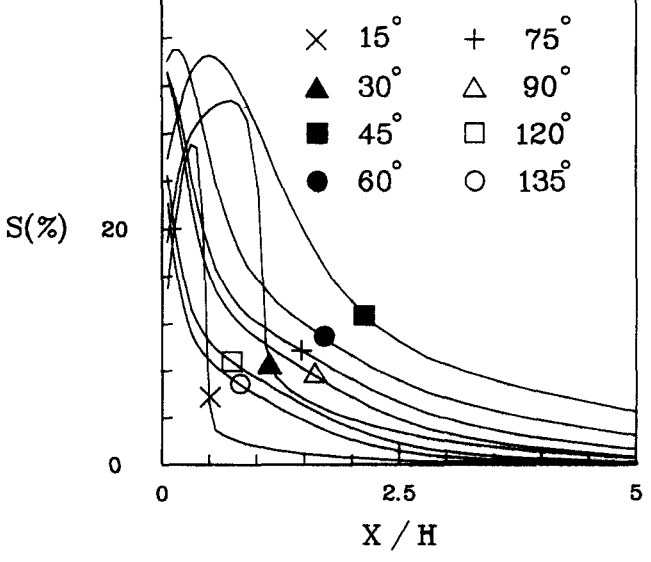

Figure 7 Calculated deviation of fuel concentration distribution at each axial station for various θ (A/F = 4.0, Re = 1.89×10^4)

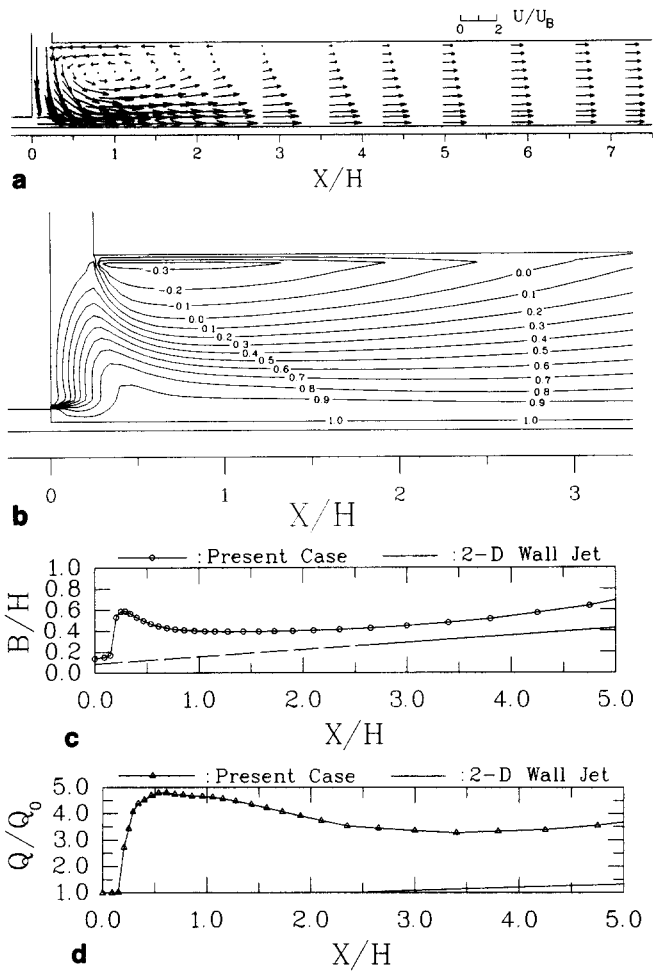

Figure 8 (a) Mean-velocity vector plot; (b) mean-velocity contour plot; (c) streamwise variation of fuel-jet width; (d) rate of fuel-jet mass entrainment ($\theta = 90°$, A/F = 4.0, Re = 1.75×10^4)

Figures 9 and 10. It is seen that the measured temperature profiles at both axial- and side-inlet ports are rather uniform. The corresponding mean-velocity profile is top-hat shaped at the side-inlet port due to 10.3:1 contraction located upstream and is fully developed at the axial-inlet port due to the longer distance between the contraction section and the axial-inlet port. Note that the solid curve in Figure 10 denotes the 1/7-power law profile and is in close agreement with the experimental data. Consequently, the inlet condition at the side-inlet port can be characterized as fully developed turbulent flow. In contrast, the measured axial-inlet mean-velocity profile only can be fitted by a 1/11.7-power law (Figure 9) and is approximately top-hat shaped. Also note that all the curves under the dimensionless coordinates shown in Figures 9 and 10 reveal similarity with respect to the range of A/F interested. Corresponding to A/F = 3.4, 4.0, 4.6, are $U_{max} = 24.4$, 22.1, 24.9 m/sec and $V_{max} = 19.0$, 15.1, 14.0 m/sec, respectively.

Inside the combustor, the results measured by using Mach-Zehnder interferometry and thermocouples are compared with the computed results in Figures 11b–13 for three typical A/F. Before these figures, Figure 11a is a typical image-processed photograph of the infinite fringe interferograms obtained by using Mach-Zehnder interferometry. The fringes in this type of interferograms correspond to isothermal lines. From these interference fringes the corresponding fuel concentration contours (Figure 11b) and profiles at various axial stations (Figures 11b–13) can then be deduced. It is seen that the measured and predicted results are in reasonable agreement for all three cases. In general, the quantitative discrepancy between the laser interferometric and computed fuel concentration contours or profiles for the range of A/F interested is within 16 percent and between the thermocouple data and computed results is within 20 percent, respectively. In addition, the discrepancy between the results measured by the two experimental methods is normally within 15 percent. The discrepancies among the results obtained by the three methods adopted in the present work are larger in the region where steep concentration gradients prevail since 3-D effect often appears in these regions, as revealed by Figure 14. In these regions, the thermocouple measurements were first performed across the chamber width and then the measured results were averaged over the width.

Effect of air-to-fuel mass ratio

The effect of the air-to-fuel mass or momentum ratio on the mixing pattern in the combustor investigated may be illustrated from Figures 12–14. Basically, the overall mixing pattern is qualitatively a weak function of A/F. That is, for the range of A/F interested, steep concentration gradients all occur in the interaction layer between the air and fuel streams and decay toward the downstream directions. Additionally, all three figures depict uniform concentration distribution on the upper wall side due to the presence of the large recirculation zone, as shown previously in Figure 3.

On the other hand, as mentioned above, the uniformity of mixing may be expressed in terms of the S value. The effect of A/F on the streamwise variation of S can then be studied from

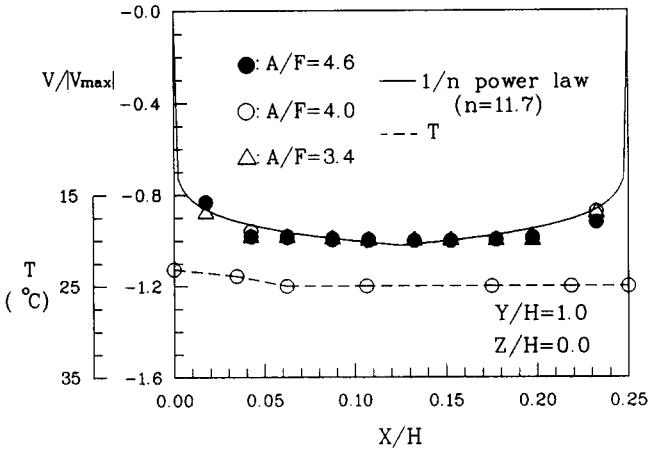

Figure 9 Measured mean velocity and temperature profiles at side-inlet port for three typical A/F

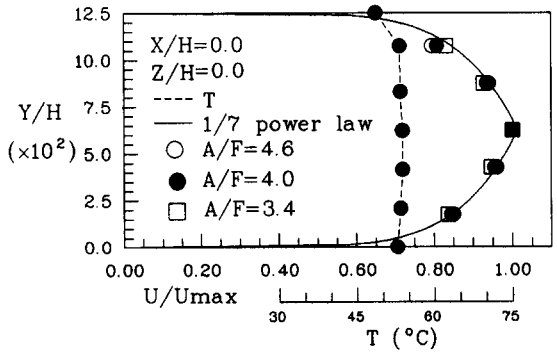

Figure 10 Measured mean velocity and temperature profiles at axial-inlet port for three typical A/F

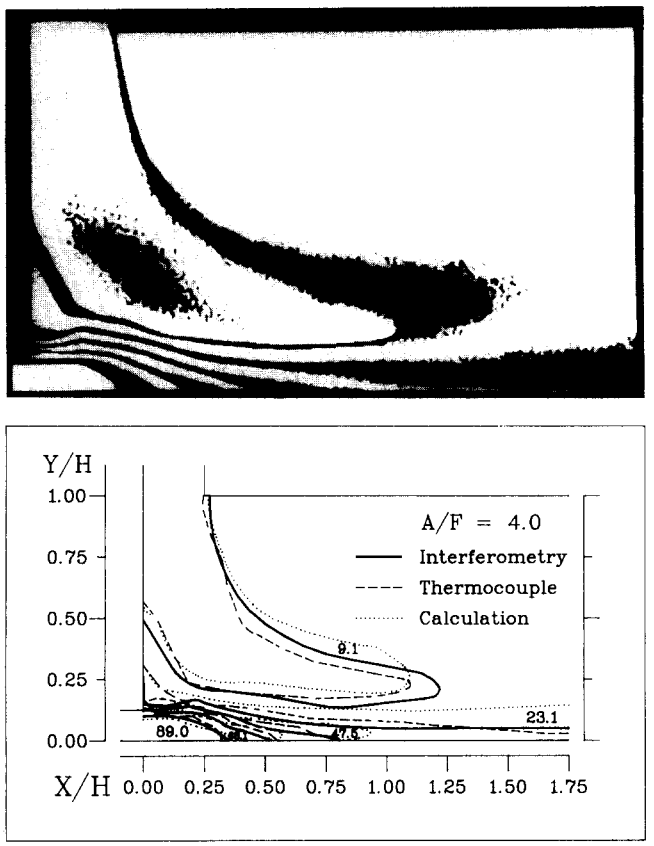

Figure 11 (a) A typical photograph of laser Mach-Zehnder interferometric fringes; (b) calculated and measured fuel concentration contours ($\theta = 90°$, $Re = 1.75 \times 10^4$)

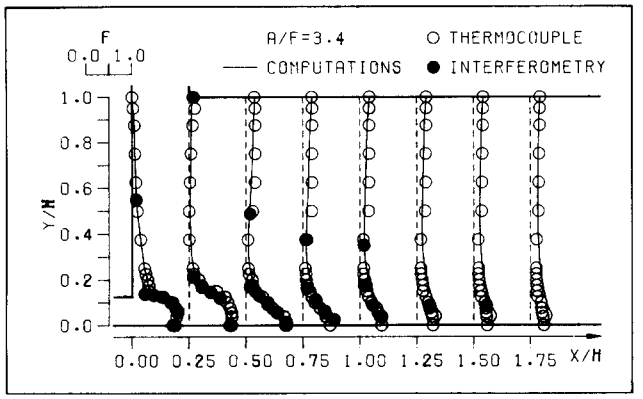

Figure 12 Calculated and measured fuel concentration profiles at various axial stations ($\theta = 90°$, $Re = 1.75 \times 10^4$)

Figure 15. Again, the uniformity of mixing increases with increasing X/H for all A/F investigated. This trend can also be seen from a comparison of Figure 12 with Figure 13. Moreover, at a given X/H, the uniformity of mixing increases with increasing A/F since the strength of jet impingement increases with increasing A/F for a fixed side-inlet angle.

Effect of Reynolds number

For $\theta = 90°$ and A/F = 4.0, a typical variation of the measured fuel concentration profile with the Reynolds number is depicted in Figure 16. Similar to the case of coaxial mixing in an industrial furnace studied previously by Khalil,[3] the combustor Reynolds number has very weak effect on the concentration distribution as long as the combustor Reynolds number is sufficiently high, $Re \geq 1.75 \times 10^4$ for the present case. The phenomena observed above may be due to the insensitivity of the recirculating zone to the variation of Reynolds number for $Re \geq 1.75 \times 10^4$. The calculated reattachment length was found to be approximately constant with a value of $(3.1 \pm 0.3)H$ for the range of Reynolds number interested.

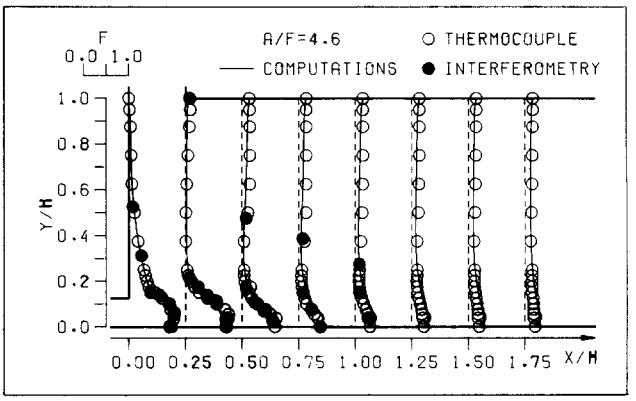

Figure 13 Calculated and measured fuel concentration profiles at various axial stations ($\theta = 90°$, $Re = 1.75 \times 10^4$)

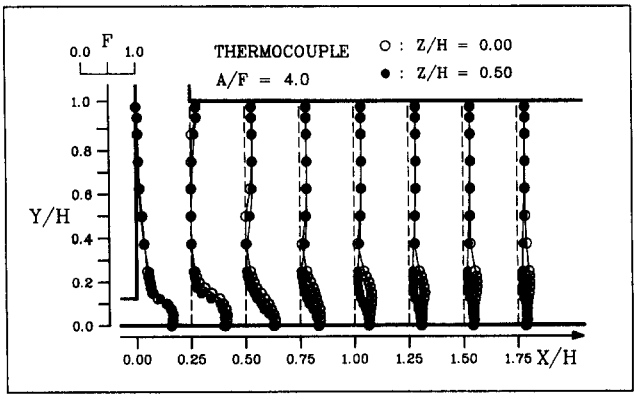

Figure 14 Measured fuel concentration profiles at various axial stations for two different z/H planes ($\theta = 90°$, $Re = 1.75 \times 10^4$)

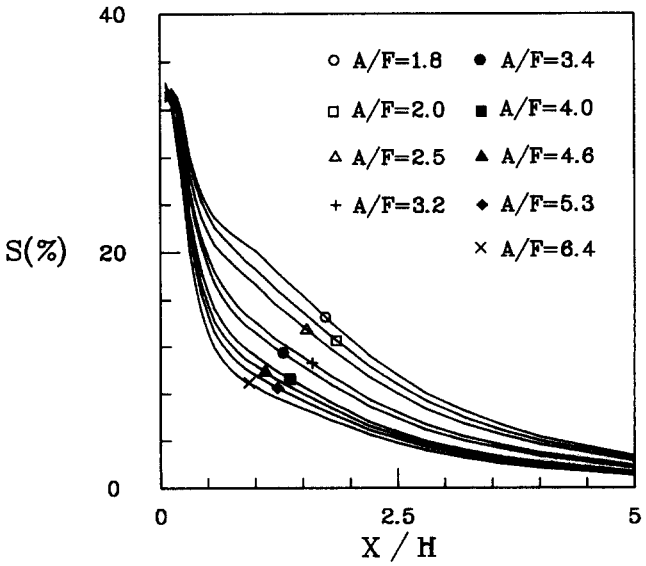

Figure 15 Effect of A/F on the streamwise variation of uniformity of mixing ($\theta = 90°$, $Re = 1.75 \times 10^4$)

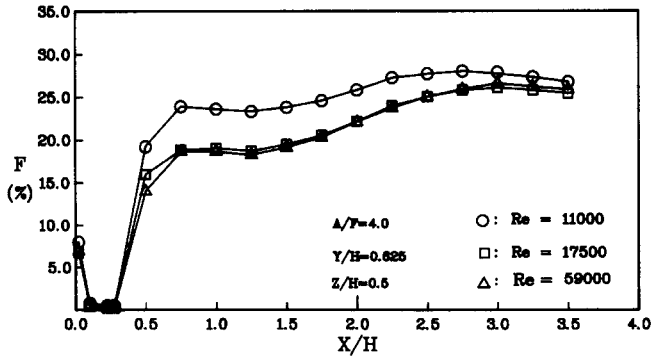

Figure 16 Variation of measured fuel concentration profile with Reynolds number ($\theta = 90°$)

Data accuracy

For the case of thermocouple probing measurements, the correction made for the heat conduction loss along the thermocouple wires is generally within 0.4 K or the corresponding mixture fraction of 2 percent. The stagnation correction is negligible due to the low Mach number of the flow. The uncertainties in laser Mach-Zehnder interferometry measurements are normally within 5 percent. These are in part due to the difficulty in locating the fringes and in part statistical. Additional errors that need to be accounted for are end-effect errors caused by the test section that is not 2-D throughout its complete width and refraction errors caused by the gradient of temperature perpendicular to the windows. Following the procedure recommended by Goldstein,[23] the end-effect and refraction errors are negligibly small for the most part of the test section, except in the shear layer of fuel stream where errors of 3.7 percent and 1.9 percent are found for the former and the latter, respectively.

Summary and conclusions

The utility of laser Mach-Zehnder interferometry and thermocouple probing in the quantitative measurements of scalar mixing in confined noncoaxial jets has been made. The measured results are in good agreement with the computed results using the algebraic Reynolds stress turbulence model.

The flow and mixing patterns in the side-dump combustor investigated depend strongly on the side-inlet angle. There exists a critical side-inlet angle, $\theta = 45°$, below which the position of the large recirculating zone is shifted from the upper wall side to the bottom wall side and the number of recirculating zones increases with decreasing θ. Moreover, the size of the large recirculating zone and the uniformity of mixing increase and the flame length in the reacting case may decrease with increasing θ for $\theta > 45°$ and with decreasing θ for $\theta < 45°$. The presence of the critical θ is due to the transition of the dominant mechanism for the flow field from jet impingement to jet entrainment.

Additionally, at a given combustor Reynolds number and axial station, the uniformity of mixing increases with increasing A/F due to increasing strength of jet impingement. At a given A/F, as long as the combustor Reynolds number is sufficiently high, the size of recirculating zone and hence the fuel concentration distribution are found to depend weakly on Reynolds number.

References

1 Schetz, J. A., and Thompson, B. D. Water flow tests of a ducted rocket combustor. *AIAA* paper AIAA-85-1107, 1985

2 Broman, G. E., and Zukoski, E. E. Experimental investigations of flame stabilization in a deflected jet. *9th International Symposium on Combustion*. Academic Press, New York, 1963, 944–956

3 Khalil, K. H. *Flow, Mixing and Heat Transfer in Furnaces*. Pergamon Press, Elmsford, NY, 1978, 1–64

4 Reuter, D., Daniel, B. R., Jagoda, J. I., and Zinn, B. T. Periodic mixing and combustion in gas fired pulsating combustors. *Combustion and Flame*, 1986, **65**, 281–290

5 Moon, L. F., and Rudinger, G. Velocity distribution in an abruptly expanding circular duct. *ASME Journal of Fluids Engineering*, 1977, **99**, 226–230

6 Yang, B. T., and Yu, M. H. The flowfield in a suddenly enlarged combustion chamber. *AIAA J.*, 1983, **21**, 92–97

7 Chen, L., and Tao, C. C. Study on the side-inlet dump combustor of solid ducted rocket with reacting flow. *AIAA* paper AIAA-84-1378, 1984

8 Vanka, S. P., Craig, R. R., and Stull, F. D. Mixing, chemical reaction and flow field development in ducted rockets. *AIAA* paper AIAA-85-1271, 1985

9 Cherng, D. L., Yang, V., and Kuo, K. K. Simulations of three-dimensional turbulent reacting flows in solid-propellant ducted combustors. *AIAA* paper AIAA-88-3042, 1988

10 Hwang, Y. H. Theoretical analysis on flow fields in side inlet dump combustors. Ph.D. Thesis, Dept. Power Mech. Eng., National Tsing Hua University, Hsin-Chu, Taiwan, ROC, 1989

11 Schadow, K. C., and Chieze, D. J. Water tunnel and windowed combustion as tools for ducted rocket development. *1981 JANNAF Combustion Meeting*, CPIA-PUB-340-VOL-II, 1981, 101–115

12 Zetterström, K.-A., and Sjöblom, B. An experimental study of side dump ramjet combustors. *7th International Symposium on Air Breathing Engines*, ISABE paper 85-7024, 1985

13 Stull, F. D., Craig, R. R., Streby, G. D., and Vanka, S. P. Investigation of a dual inlet side dump combustor using liquid fuel injection. *AIAA Journal of Propulsion and Power*, 1985, **1**, 83–89

14 Liou, T.-M., and Wu, S. M. The flow field in a dual inlet side-dump combustor. *AIAA Journal of Propulsion and Power*, 1988, **4**, 53–60

15 Liou, T.-M., and Hwang, Y. H. Calculation of flow fields in side-inlet ramjet combustors with an algebraic Reynolds stress model. *AIAA Journal of Propulsion and Power*, 1989, **5**, 686–693

16 Liou, T.-M., Wu, S. M., and Hwang, Y. H. Experimental and theoretical investigations of turbulent flow in a side-inlet rectangular combustor. *AIAA Journal of Propulsion and Power*, 1990, **6**, 131–138

17 Spalding, D. B. *Combustion and Mass Transfer*, Chap. 6. Pergamon Press, 1979

18 Hauf, W., and Grigull, U. Optical method in heat transfer. *Advances in Heat Transfer* (Harttnett, J. P., and Irvine, T. F., Jr., eds.). Academic, New York, 1970, **6**, 133–136

19 Liou, T. M., and Hwang, J. J. Heat transfer study of turbine blade cooling channel using real-time laser holographic interferometry. *Proc. Sixth National Conference on Mechanical Engineering*, Tainan, Taiwan, ROC, 1989, 439–450

20 Launder, B. E., and Spalding, D. B. The numerical computation of turbulent flows. *Computer Methods in Applied Mechanics and Engineering*, 1974, **3**, 269–289

21 Dutt, J. C. Fundamental modeling of reacting flow in ramjet dump combustors. AFOSR-TR-81-0597, 1980

22 Liou, T. M., and Tai, J. Y. Computational and experimental study of tunnel draft with side injection of air. *Proc. Thirteenth National Conference on Theoretical and Applied Mechanics*, Taichung, Taiwan, ROC, 1989, 1185–1196

23 Goldstein, R. J. Optical techniques for temperature measurements. *Measurements in Heat Transfer* (Eckert, E. R. G., and Goldstein, R. J., eds.). McGraw-Hill, New York, 1976